ORIGINAL ARTICLE

lajss.org
Latin American Journal of Solids and Structures

www.lajss.org

Multi-objective optimization of aluminum foam-filled battery boxes for electric vehicle safety

İsmail Yay[a], Emre Demirci[a,b*], Ahmet Remzi Özcan[c]

[a]Department of Mechanical Engineering, Bursa Technical University, Bursa, 16310, Turkiye. Email: ismlyay@gmail.com, emre.demirci@btu.edu.tr
[b]Automotive Application and Research Center, Bursa Technical University, Bursa, 16310, Turkiye.
[c]Department of Mechatronics Engineering, Bursa Technical University, Bursa, 16310, Turkiye. Email: ahmet.ozcan@btu.edu.tr

* Corresponding author

https://doi.org/10.1590/1679-7825/e8408

Abstract

In this study, a multi-objective optimization methodology is used to assess the crashworthiness of an aluminum foam-filled battery box designed for passenger cars. Unlike most research focusing on axial crushing, this work investigates the less-explored side pole impact scenario in electric vehicle battery boxes. Finite element simulations are conducted to reduce peak crushing force (PCF) and increase specific energy absorption (SEA) compared to the initial design. Key design variables include aluminum foam densities, wall thickness, and cross-sectional dimensions of battery box components. Four surrogate models are evaluated to approximate the simulation results, and the Non-Dominated Sorting Genetic Algorithm (NSGA-II) is employed to achieve optimal outcomes. The results show that the optimized design significantly improves crashworthiness, achieving a 50.71% increase in SEA and an 11.56% reduction in PCF. Foam density plays a crucial role in controlling deformation behavior under impact conditions. These findings offer a new approach to designing battery boxes with enhanced crashworthiness for electric vehicles.

Keywords

Aluminum foam, battery box, crashworthiness, electric vehicle, multi-objective optimization

Graphical Abstract

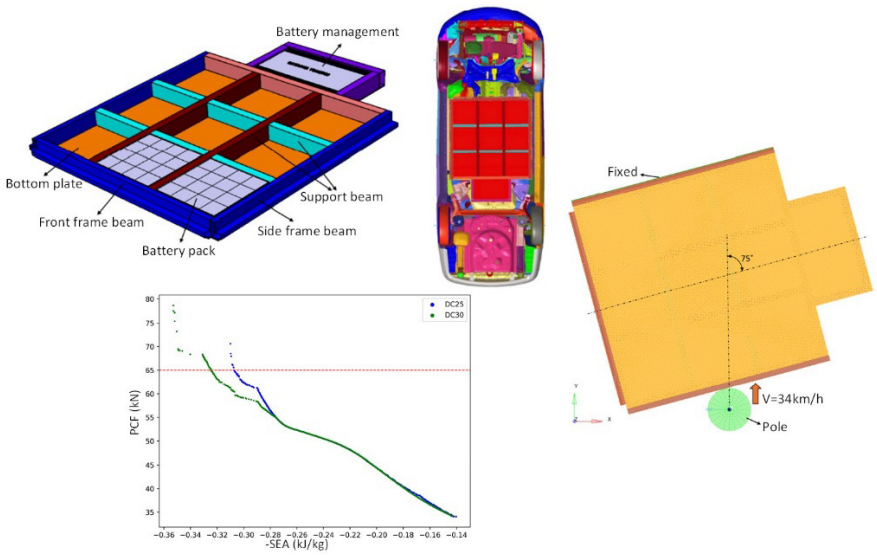

Received: out. 18, 2024. In revised form: jan. 22, 2025. Accepted: fev. 03, 2025. Available online: fev. 04, 2025
https://doi.org/10.1590/1679-7825/e8408

Latin American Journal of Solids and Structures. ISSN 1679-7825. Copyright © 2025. This is an Open Access article distributed under the terms of the Creative Commons Attribution License, which permits unrestricted use, distribution, and reproduction in any medium, provided the original work is properly cited.

1 INTRODUCTION

The widespread use of electric vehicles (EV) in recent years has led to new research and development topics in the automotive industry. One of the most important of these issues is undoubtedly battery safety. Many structures in automobiles are categorized as crash energy-absorbing elements for vehicle passive safety. In the traditional automotive industry approach, the primary focus of crashworthiness assessment is on energy absorbing structures such as bumpers, crash boxes and pillars (Abdullah et al., 2020; Safari et al., 2018; Sun et al., 2018). On the other hand, in the case of side or frontal impact scenarios, the battery boxes are also expected to act as crash elements, minimizing potential battery damage (Gong et al., 2021; Victor Chombo et al. 2021). Most of the studies on battery boxes in the literature focus on energy efficiency and cooling of battery boxes (Arora et al. 2016; Sharma and Prabhakar, 2021). However, studies on the mechanical design, lightweighting and crashworthiness of the battery case are relatively few. Yang et al. investigated the behavior of a finite element (FE) model of a battery box under bumpy road, sharp curve, and sudden braking conditions (Yang et al., 2019). They performed static strength analysis on the battery box for various loading conditions. In addition, the modal properties and vibration of the battery box were analyzed, and the performance of the battery box was comprehensively examined, leading to improvements in its weak points. In another study, the mechanical behavior of the designed battery box in various vehicle collision scenarios was investigated (Navale et al., 2021). In order to achieve better crash performance in tests conducted in accordance with Euro NCAP norms, various design modifications were implemented, including the redesign of different structural elements such as front rails, cross members, subframe, door sill area. In a different study, a side collision was considered in the crashworthy design developed in accordance with the Euro NCAP standard and an impact energy absorbing foam filling material and aluminum honeycomb structure were proposed to be applied on the sides of the batteries to reduce the risk of battery explosion (Setiawan and Salim, 2017). In a recent publication, Farzaneh et al. presented a novel design for strengthening structural integrity and improving the thermal regulation of EV batteries. This design employs thin-walled aluminum tubes filled with phase change material (PCM) (Farzaneh et al., 2024).

The majority of studies on crashworthiness have concentrated on two key elements: improving safety performance and reducing weight through lightweight design. To achieve these two seemingly contradictory goals, one of the issues researchers are focusing on is new-generation materials (Magliaro et al., 2022; Yao et al., 2023). A wide range of materials have been investigated, including new generation steels (Doruk and Demir, 2024; Erzincanlioğlu et al., 2022), lightweight alloys (Demirci and Yıldız, 2018; Li et al., 2024a), composites (Mou et al., 2016; Li et al., 2024b), bio-inspired materials (Huang et al., 2022; Saber et al., 2024) and metallic foams (Djamaluddin et al., 2016; Linul et al., 2021) all aimed at developing weight-reduced crashworthy structures. Aluminum alloy materials are extensively utilized in the automotive industry for lightweight design and crashworthiness applications. The use of aluminum alloys in lightweight design aligns with the automotive industry's requirements for improved fuel efficiency, reduced emissions, and enhanced vehicle performance (Chen, 2023). Aluminum alloys offer advantages such as a high strength stiffness-to-weight ratio, good formability, and recyclability, making them suitable replacements for heavier materials like steels in vehicles to meet weight reduction demands (Kovács and Lukács, 2022). In terms of crashworthiness, thin-walled aluminum alloy structures are essential for industries requiring high energy absorption efficiency and lightweight components, including the automotive sector (Demirci and Yıldız, 2018; K. Li et al., 2020). The hybridization of aluminum with materials like carbon fiber-reinforced composites is considered a novel design concept that fulfills the requirements for lightweight construction and crashworthiness in automotive applications (Bidadi et al., 2024). The use of carbon fiber-reinforced aluminum matrix composites is also gaining traction, as these materials combine the light-weight properties of aluminum with the high strength of carbon fibers, leading to improved crash performance (Yu and Jiang, 2024). Moreover, aluminum foam materials have garnered significant attention in the automotive industry, particularly for their potential to enhance crashworthiness. These materials exhibit unique properties that make them suitable for energy absorption and structural reinforcement during impact events. An et al. (2012) indicates that aluminum foams exhibit a high strength-to-weight ratio, allowing them to sustain large plastic deformations under compressive loading, which is crucial for absorbing substantial impact energy compared to conventional materials. Additionally, aluminum foam-filled structures have been shown to improve crash performance by providing better stability and energy absorption characteristics, making them suitable for applications in crashworthiness structures (Fragoso-Medina and Velázquez-Villegas, 2023; Sharma et al., 2022). Altin et al. (2017) conducted an experimental study to investigate the energy absorption capacity of thin-walled square and circular tubes with different ratios of foam filling in axial compression. Their findings emphasized that foam-filled designs exhibited enhanced specific energy absorption and crushing force efficiency performance values compared to unfilled designs. Neu et al. (2024) explores the potential of aluminum foam sandwiches (AFS) as lightweight materials for automotive applications. The study emphasizes that AFS can significantly contribute to weight reduction, and they are suitable for structural applications in EV battery boxes and car bodies.

Baumeister et al. (2014) found that aluminum hybrid foam sandwiches (AHFS) offer significant advantages in crashworthiness and weight reduction compared to traditional materials, enhancing energy absorption during collisions to protect battery modules from damage. The study highlights that AHFS achieve an optimal balance between lightweight design and structural integrity, making them well-suited for use in battery housings for electric vehicles.

Structural optimization is another area of focus for researchers to improve safety performance and reduce weight through lightweight design. Current advancements in structural optimization, particularly in the context of crashworthiness, emphasize the integration of multi-objective and robust optimization methods. These approaches are essential in developing designs that balance the demands of safety and efficiency, as highlighted by recent studies in the field (Fang et al., 2017). Multi-objective optimization techniques, such as multi-objective particle swarm optimization (MOPSO) and nondominated sorting genetic algorithms (NSGA), have proven highly effective in addressing the complex trade-offs in crashworthiness design by optimizing criteria like energy absorption, weight reduction, and peak deceleration (Liao et al., 2008a; Sun et al., 2011). Surrogate modeling approaches, such as Kriging and response surface methodology (RSM), play a crucial role in approximating complex crashworthiness functions, reducing computational costs, and handling nonlinearities effectively (Kurtaran et al., 2002; Liao et al., 2008a; Raponi et al., 2019). These advanced optimization strategies have been successfully applied across various structures, such as thin-walled structures (Yildirim et al., 2023; Yıldız, 2020), cellular structures (Albak, 2023; Wang et al., 2023), foam-filled structures (Djamaluddin, 2024; Meriç and Gedikli, 2022), composite and functional gradient materials (Gao and Huaiwei, 2023; Zhou et al., 2022) to improve crash performance. There are only a few studies in the literature on the optimization of battery boxes for electric vehicles. Qiao et al. (2021) explored the safety improvement of battery boxes in side collisions by introducing design optimizations, such as evenly distributing bosses around the battery box and adding interlocking structures between the upper and lower parts. Their finite element analysis demonstrated significant reductions in stress and deformation during side impacts. Wang et al. (2024) focused on multi-objective lightweight design for battery pack enclosures, using the NSGA-II algorithm and the TOPSIS method to reduce both weight and deformation. In the study by Biharta et al. (2022), the researchers developed a lightweight and crash-resistant battery protector using 3D auxetic structures. These auxetic materials enhance energy absorption and deformation resistance, leading to improved safety during impacts, while also reducing the overall weight. In an other study, the researchers developed a modified particle swarm optimization algorithm for optimizing the reliability of composite battery boxes, focusing on both structural integrity and lightweight design (Liu et al., 2018).

This paper advances the crashworthiness optimization of aluminum foam-filled battery boxes for electric vehicles by implementing a robust multi-objective framework. Unlike many studies that focus on axial crushing, especially in the context of conventional crash boxes, this research addresses the critical but less explored side pole impact scenario for electric vehicle battery boxes, aiming to enhance specific energy absorption (SEA) and reduce peak crushing force (PCF). The need to address this specific scenario arises from the increasing prevalence of electric vehicles, where battery systems play a central role in both vehicle functionality and safety. While side pole impacts have been widely studied for conventional vehicles, their implications for electric vehicles remain underexplored, particularly due to the unique structural and safety requirements of battery enclosures. By focusing on this underexplored area, the study aims to provide actionable insights that contribute to both the academic understanding and practical design of safer EV battery systems. To achieve this objective, a numerical model is developed using the finite element method (FEM) to simulate the crashworthiness performance of the battery box under side pole impact conditions. Key design variables, such as the thicknesses of the battery box components, aluminum foam densities, and shape parameters, are optimized using the Non-Dominated Sorting Genetic Algorithm (NSGA-II). Additionally, various surrogate modeling techniques, including Response Surface Methodology (RSM), Kriging, Radial Basis Function (RBF), and Support Vector Regression (SVR), are employed to model complex relationships between the design variables and crashworthiness outcomes. By evaluating the prediction performance of these surrogate models, the research identifies the most reliable and efficient models for the optimization process. This comprehensive approach not only improves the crash performance of battery boxes but also fills a gap in the literature by addressing side impact conditions, particularly for electric vehicles, offering practical insights for enhancing the safety of these battery systems.

2 MODELLING OF THE BATTERY BOX AND CRASH SIMULATION

2.1 Geometric Description

A review of the literature on vehicle battery box design revealed that the front and side sections of the battery box outer frame are typically constructed with an "L" profile (Bala and Chaitanya Kamaraju, 2020; Navale et al., 2021; Safari et al., 2018). One of the most significant advantages of this design is that it enhances the vehicle’s crash resistance.

The battery separator and support beams located within the interior of the structure are typically designed with rectangular profiles. In this study, a battery box model, depicted in Figure 1a, is devised through the utilization of computer-aided design software, with due consideration given to the fundamental design elements as elucidated in the extant literature. The battery box comprises a number of key components, including top and bottom plates, side and front frame beams, support beams, and a dedicated battery management section. Battery cell packs are not included in the finite element (FE) analyses. The design of the battery box model is based on the dimensions of a passenger car as a dimensional constraint. For this purpose, since there is no accessible finite element model of an electric vehicle, the dimensions of the Toyota Yaris developed by the National Crash Analysis Center (NCAC) (Marzougui et al., 2013), which has an internal combustion engine, are used as a basis. The outer frames of the battery box have been designed to fit into an area measuring 1300×1235mm. The layout of the battery box as it is to be positioned on the vehicle is illustrated Figure 1b.

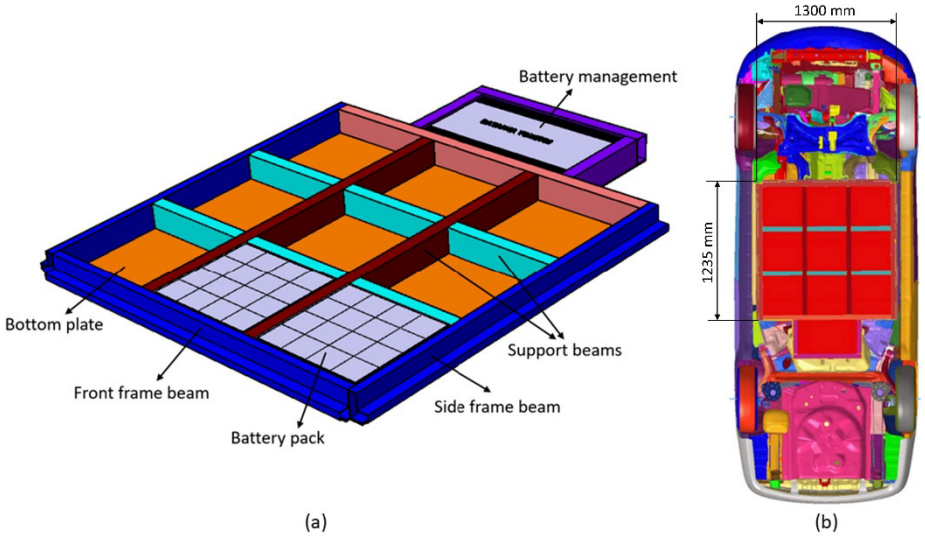

Figure 1 Battery box design (a) components (b) layout on the vehicle and outer dimensions.

Due to the considerable number of mesh elements in the finite element model of the vehicle and the high computational cost of the numerical solution, the crash analyses conducted solely with regard to a side impact on the battery box, rather than on the vehicle as a whole. Figure 2 illustrates the cross-sectional view of the "L" beam utilized in the construction of the battery box outer frame. The "L" beam is designed with a height of 70 mm and a width of 60 mm. The frame wall thickness (t_1) and x_1, x_2 and x_3 lengths are defined as the design variables.

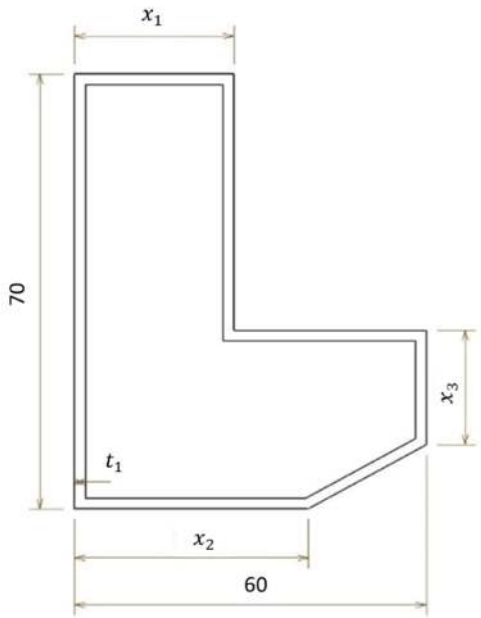

Figure 2 Cross-sectional view of the 'L' beam and design variables (All dimensions are in millimeters).

2.2 Crashworthiness Criteria

A number of criteria are used to assess the performance of structural components subjected to a crash (Albak, 2021; White and Jones, 1999). Among these criteria, energy absorption (EA), specific energy absorption (SEA), and peak crushing force (PCF) are some of the most common and are used in this study. EA refers to the total amount of kinetic energy that a structure or material can dissipate during deformation under an external load, typically during an impact or crash scenario. It is a critical parameter in crashworthiness analysis as it reflects the capability of a system to reduce the intensity of forces transmitted to occupants or sensitive components. It can be expressed mathematically as:

$$EA = \int F(x)dx \tag{1}$$

where $F(x)$ is the force as a function of displacement x, and the integral is taken over the range of deformation. Specific energy absorption (SEA) is a normalized measure of a structure's energy absorption capacity per unit mass. It is used to evaluate the efficiency of lightweight structures in crashworthiness applications, particularly in the automotive and aerospace industries. The expression for SEA is:

$$SEA = EA / m \tag{2}$$

where m is the mass of the structure or material. PCF is the maximum force experienced by a structure during the initial phase of deformation under a crushing load, which can be written as:

$$PCF = \max(F(x)) \tag{3}$$

In the context of crashworthiness, PCF is a critical factor, as excessively high forces can lead to catastrophic failure or increased risk of injury. The goal in designing crashworthy structures is to lower the peak crushing force while maintaining adequate energy absorption, thereby controlling the force transmission during impact.

2.3 Finite Element Modelling

The crashworthiness analyses of the designed battery box are carried out by finite element method (FE) using Radioss, an explicit dynamic finite element solver (Altair Hyperworks, 2019). Battery box sections are typically thin-walled structures. The aluminum foam materials mounted on the front and side frames of the battery box are defined as solid structures. All shell elements are designed as mid-surfaces, thereby allowing the thickness to be modified parametrically. The mesh structure of the shell elements is created using four-node shell elements (type quad4) with five integration points through the thickness. The mesh structure of the solid aluminum foam model is created using 8-node solid elements. The dimensions of the mesh structure are closely related to the accuracy of finite element analysis. In general, decreasing the size of the mesh structure results in more accurate analysis results. Nevertheless, an excessive reduction in the mesh size has the effect of considerably extending the solution time, which in turn results in the loss of time and an increase in the computational cost. The battery box model used in this study is designed based on the dimensions of a full-scale finite element model of a Toyota Yaris vehicle. In the original vehicle model, a global mesh size of 10 mm is applied for the structural components. Following this approach, a mesh convergence analysis is performed, starting with a mesh size of 10 mm and progressively refining it in steps of 2.5 mm down to a minimum of 2.5 mm. Four different mesh sizes (10 mm, 7.5 mm, 5 mm, and 2.5 mm) are examined to evaluate the effect of mesh refinement on SEA and computational cost. The results of the mesh convergence analysis are presented in Figure 3. As shown, SEA values exhibited minimal variation across different mesh sizes, indicating that further refinement beyond a certain level does not significantly enhance accuracy. However, the computational time (CPU time) increased substantially as the mesh size decreased, with the smallest mesh size requiring the highest computational resources. Since the optimization process involves dynamic mesh updates using HyperMorph, using a very large mesh size would lead to significant mesh distortion, negatively affecting the accuracy of the results. On the other hand, employing a very fine mesh size would result in excessive computational cost. Based on these considerations, a global mesh size of 5 mm is selected as the optimal balance between accuracy and computational efficiency.

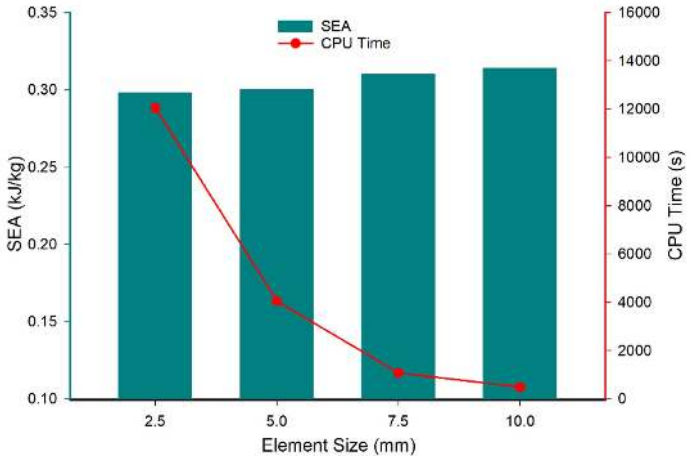

Figure 3 Mesh convergence analysis

Figure 4 illustrates the views of the mesh structures of the shell and solid components. Node to surface and edge to edge definitions are created for the contact interface of the battery box sheet metal parts and aluminum foam material with each other and with the striking pole during the crash. The assembling of the battery box sheet metal parts is carried out by point-by-point spot welding definition between the nodal points. The potential softening effect due to welding between the aluminum components was not explicitly modeled. The structural components were assumed to have uniform material properties throughout, as the focus of the study was on the overall crashworthiness optimization rather than local effects near weld zones. The finite element model assumes an idealized geometry of the battery box, which does not account for manufacturing imperfections or detailed connection elements such as screws.

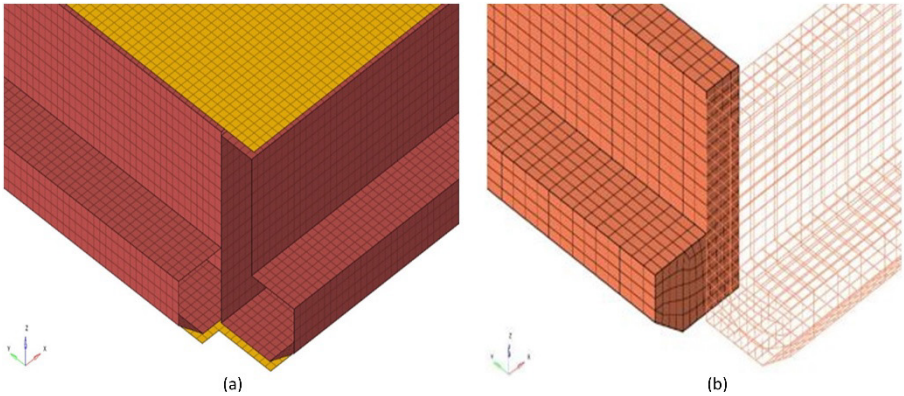

Figure 4 Mesh structure (a) frames and top-bottom plates (b) aluminum foam

In this study, a medium-strength aluminum alloy, AA7003-T1, is employed for the battery box sheet components, exhibiting the following mechanical properties: density ρ=2.770 kg/m^3, Young's modulus E=71000 MPa, yield stress σ_y=202 MPa and Poisson's ratio v=0.33. The isotropic elasto-plastic material card (MAT36) is employed to model the nonlinear behavior of the aluminum alloy material during the impact. The mechanical properties of the material are utilized to characterize the elastic region, whereas the true stress-strain curve (Kokkula et al., 2006) is employed to define the behavior exhibited in the plastic region. Three aluminum foams with densities of 0.17 g/cm^3, 0.34 g/cm^3 and 0.51 g/cm^3 are used to create the metallic foam material. The mechanical properties of aluminum foam materials are presented in Table 1 (Reyes et al., 2003). The Deshpande-Fleck foam law material card (MAT115) is used for the FE modelling of aluminum foam materials. To determine the foam material parameters, the following equation is employed, which provides the yield stress value in dependence on the hardening (Ahmad and Thambiratnam, 2009):

$$\sigma_y = \sigma_p + \gamma \frac{\hat{\varepsilon}}{\varepsilon_D} + \alpha_2 \ln\left(\frac{1}{1-\left(\frac{\hat{\varepsilon}}{\varepsilon_D}\right)^{\beta}}\right) \tag{4}$$

where σ_y is yield stress, σ_p is plateau stress, $\hat{\varepsilon}$ is equivalent strain. α_2, β and γ are material parameters. The densification strain, ε_D, obtained by uniaxial compression test is expressed as follows:

$$\varepsilon_D = -\frac{9+\alpha^2}{3\alpha^2}\ln\left(\frac{\rho_f}{\rho_0}\right) \tag{5}$$

where ρ_f is the density of the foam and ρ_0 is the density of the base material. Since aluminum foam material will be used within the scope of this study, ρ_0 value will be taken as 2.7 g/cm^3.

Table 1 Mechanical properties of the aluminum foam materials.

ρ_f	E	γ	ε_D	α_2	β	σ_p
[g/cm^3]	[MPa]	[MPa]	[MPa]	[MPa]	[MPa]	[MPa]
0.17	377	1.87	2.77	93.5	5.79	1.15
0.34	1516	3.92	2.07	60.2	4.39	5.76
0.51	5562	5.37	1.67	66.9	2.99	14.82

The battery box side crash analyses examined in this study are modelled in accordance with the Euro NCAP side pole crash standards (Euro NCAP, 2015). Therefore, a rigid pole with a diameter of 254 mm is formed and impacted at a speed of 32 km/h at an angle of 75˚ with the vehicle longitudinal centerline. In real-world side pole impact tests, the pole typically strikes the vehicle as a whole, causing damage to body in white components before transferring forces to the battery enclosure. However, in this study, the analysis is focused solely on the battery enclosure, isolated from the surrounding vehicle structure. Consequently, boundary conditions are simplified. The crash occurred through the left side frame of the battery box. Conversely, all degrees of freedom of movement are constrained on the opposite side of the battery box. FE model of the battery box subjected to pole impact. This approach ensures computational feasibility and isolates the performance of the battery enclosure itself, but it may not fully replicate the complex interactions present in a complete vehicle crash scenario. Future studies could incorporate the full vehicle structure to provide a more comprehensive understanding of the enclosure's behavior under realistic impact conditions. Figure 5 illustrates the pre-collision FE model representation of the impacting pole and battery box. The dynamic effects and thermal properties of individual battery cells are not explicitly modeled in this study. The finite element analysis focuses on the structural behavior of the battery enclosure under impact conditions, assuming that the interactions within the cells do not significantly influence the overall crashworthiness performance. This simplification reduces computational complexity while maintaining the study's focus on optimizing the structural components of the box.

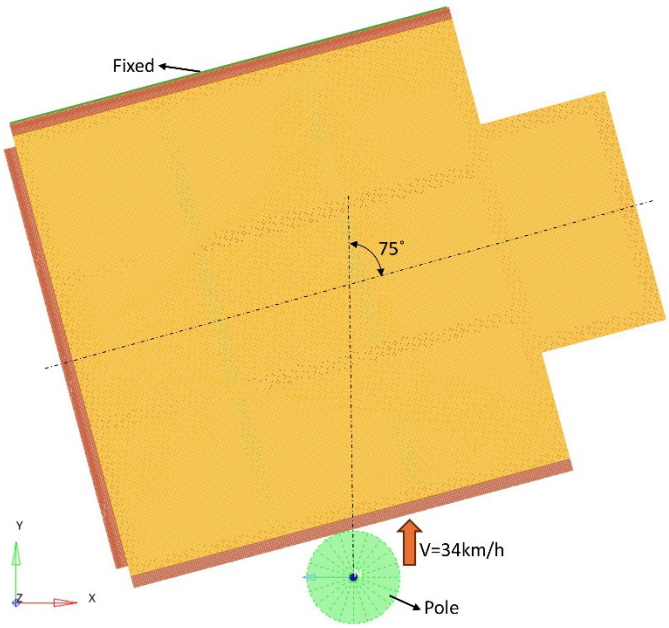

Figure 5 FE model of the battery box subjected to pole impact.

2.4 Validation of the FE Model

To ensure the accuracy of the finite element method, it is essential to compare the results of the analyses conducted with physical tests or verified numerical solutions in the literature. A FE model of the experimental tests conducted by Altin et al. (2017) is created to validate the shell elements and assess the accuracy of the model. Due to the unavailability of impact test data applied to a battery box frame, a finite element model of an empty aluminum circular tube is utilized to represent the experimental conditions. The thin-walled circular structure is designed as a cylinder with a wall thickness of 1.35 mm, a length of 100 mm, and a diameter of 75 mm, similar to the one used in the experimental test. In the quasi-static experiments conducted by Altin et al. (2017), the deformation speed of the rigid plate is applied as 2 mm/min. To simulate the impact condition in the validation study presented in this work, a rigid plate was moved in the axial direction to generate an impact force from the top of the tube, as shown in Figure 6. In this simulation, the deformation speed was selected as 2 mm/s to reduce computational cost. This approach is consistent with validation studies in the literature (Altin et al., 2018; Acar et al., 2019). The plate continued its movement until the specimen is deformed to a length of 50 mm, representing half its original length. The isotropic elasto-plastic material card (MAT36) is used for the aluminum alloy material. The interaction between the circular tube and the moving rigid plate is defined with a friction coefficient of 0.3 (Altin et al., 2017).

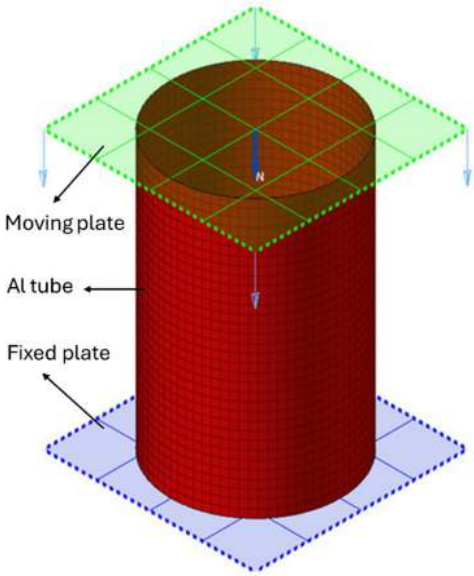

Figure 6 FE model of the thin-walled circular tube used in the validation study.

The collapse behavior of the tubes and the force-displacement curves for the validation and reference experimental studies are illustrated in Figure 7 and Figure 8, respectively. A comparison of the deformation types observed in the experimental test and the finite element model prepared for the validation study revealed a high degree of similarity in the observed crushing behavior. Furthermore, a notable correlation is observed between the shape and number of fluctuations in the curves represented in the force-displacement graph. In their experiments, Altin et al. (2017) observed that the peak crushing force (PCF) value is approximately 56.5kN. In FE analysis, the PCF value is obtained as 54.3kN. The results indicate a relative error of 3.89%, which suggests a high degree of agreement between the FE model and the test data. Additionally, the SEA value is calculated as 13.92 kJ/kg in the experimental test, while it is obtained as 13.21 kJ/kg in the validation study. This corresponds to a relative error of 5.09%, further confirming the accuracy and reliability of the finite element model in replicating the experimental observations.

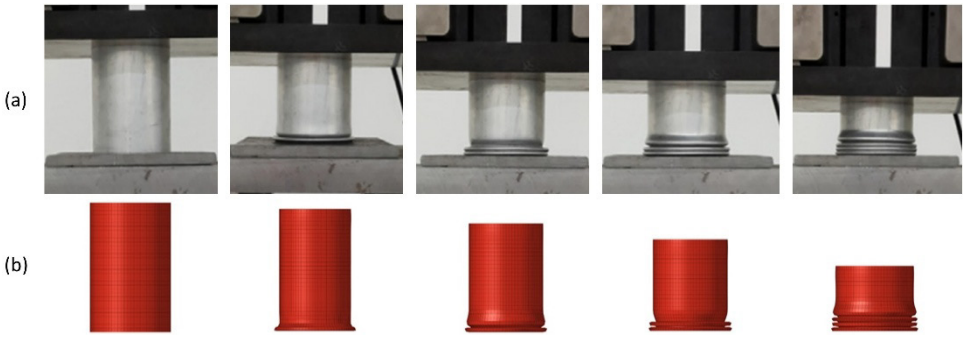

Figure 7 Comparison of deformation modes (a) experimental test (Altin et al., 2017) (b) FE model.

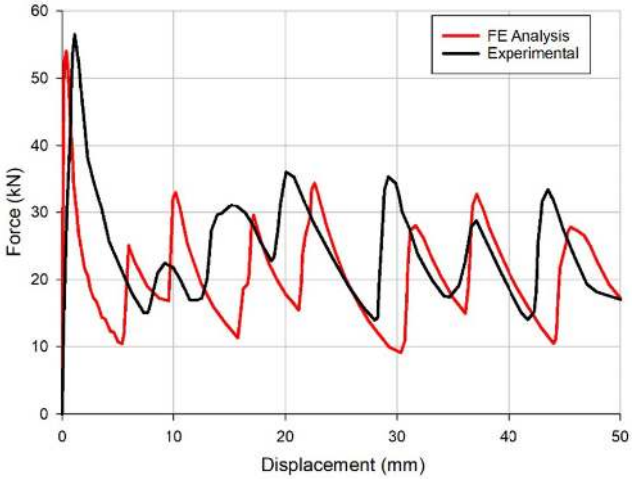

Figure 8 Force-displacement curves of FE analysis and experimental test (Altin et al., 2017).

A validation study is also carried out for aluminum foam material with different densities. Finite element models of aluminum foam materials, for which the mechanical properties are given in Table 1, are subjected to numerical compression tests and the results are compared with the findings of the experimental study (Hanssen et al., 2002). In their study, Hanssen et al. (2002) designed a cubic part with a dimension of 70x70x70 mm and positioned it on a fixed plate. The part was then subjected to quasi-static uniaxial compression loading with a moving plate applied from the upper face, at a deformation speed of 20 mm/min. In this validation study, finite element models of aluminum foam parts with the same dimensions as the experimental specimens are created using fully integrated solid elements. The foam parts are positioned with their lower faces fixed on a rigid plate, while the upper faces are compressed by a moving rigid wall at a deformation speed of 2 mm/s, as illustrated in Figure 9. This deformation speed is chosen to optimize computational cost while allowing for a feasible simulation time. The friction coefficient between the moving rigid wall and the aluminum foam is selected as 0.2, following the reference study by Reyes et al. (2003). For the aluminum foam materials, the Deshpande-Fleck foam law material card (MAT115) is utilized to accurately model their compressive behavior under uniaxial loading. As a result of the analyses, force-displacement graphs are drawn for a displacement of 50 mm and the results are compared with the curves obtained from the experimental tests. Figure 10 illustrates the force-displacement curves for three differing densities of aluminum foam material. The results of the analyses performed with 0.17 g/cm^3 and 0.34 g/cm^3 density foam materials showed high agreement with the reference study. In the FE analysis of the 0.51 g/cm^3 density foam material, the crush forces in the initial 20mm deformation distance exhibited a high degree of similarity with the experimental test results. However, due to fracture in the experimental foam specimen after 20 mm is considered to cause deviation in the results (Hanssen et al., 2002). In this study, the aluminum foam material is placed within a closed frame, which provides structural constraints that reduce localized deformation and fracture risks. Peroni et al. (2008) demonstrated that structural constraints help to control deformation and prevent fracture during compression. The frame also mitigates bending collapse mechanisms, ensuring greater stability and energy absorption. As a result, it is expected that the fracture effects observed in standalone foam tests will be significantly reduced in this configuration. It is therefore considered that FE models of aluminum foam materials are reliable and can be used in the simulations carried out in this study.

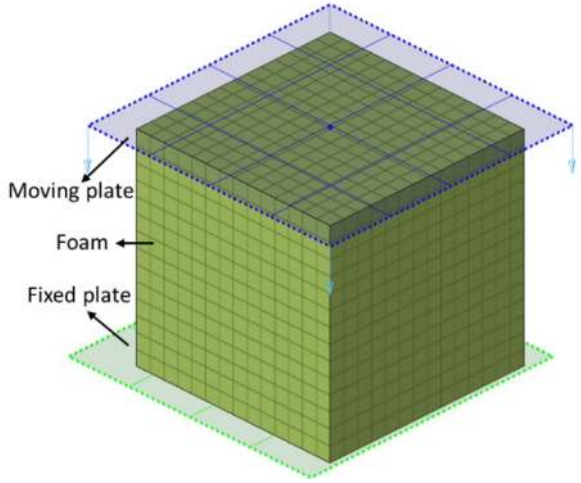

Figure 9 FE model of aluminum foam validation study.

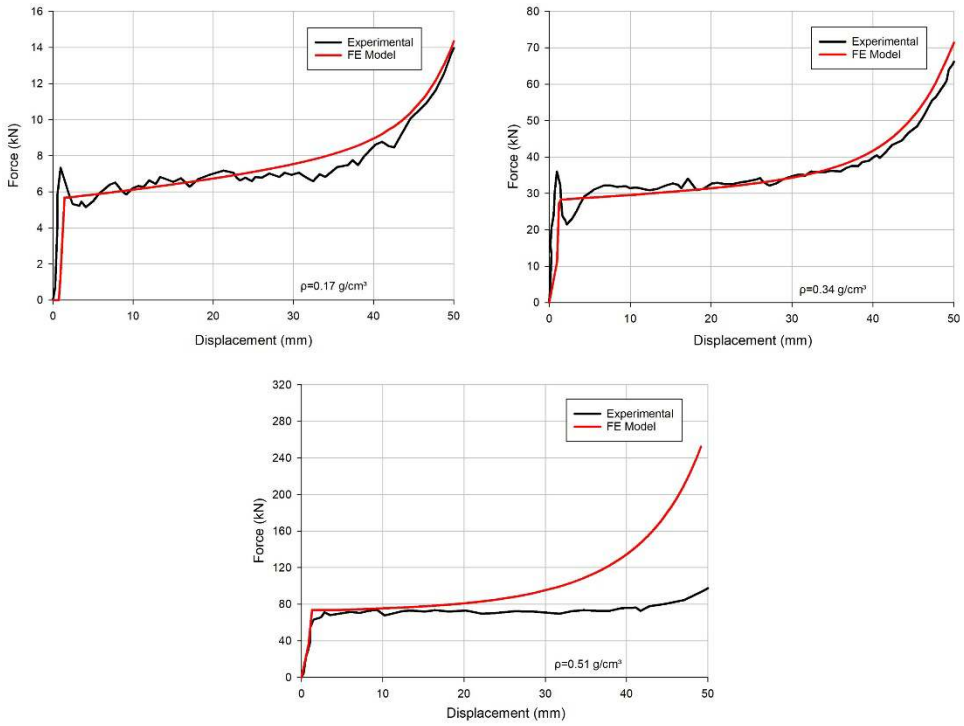

Figure 10 Comparison of experimental (Hanssen et al., 2002) and FE model force-displacement curves for aluminum foam materials.

3 OPTIMIZATION DESIGN

3.1 Definition of Optimization Problem

The objective of optimizing the aluminum foam-filled battery box for electric vehicles is to enhance its crashworthiness. This involves balancing two primary objectives: maximizing the energy absorption during a crash and minimizing the peak force experienced by the battery box. Achieving this balance is crucial for ensuring the safety of both vehicle occupants and the structural integrity of the battery box.

In this study, seven design variables are identified to achieve the objectives. The first three variables are dimensional parameters related to material thickness. These are the frame wall thickness (t_1), the support beam wall thickness (t_2), and the bottom-top plate thickness (t_3), as illustrated in Figure 11. These parameters are considered continuous variables, with a lower limit of 1 mm an upper limit of 2 mm, and an initial value of 1.5 mm. In a side impact, the structural element that first encounters the effect on the battery box is the side frame beam. The lengths x_1, x_2, x_3 on the side frame beam, as illustrated in Figure 2, are defined as shape variables, with their respective limits specified in Table 2. For the aluminum foam material, foam densities of 0.17, 0.34 and 0.51 g/cm^3 have been determined as discrete design variables. To ensure the design meets necessary safety standards and maintains structural feasibility, two constraints have been imposed on the design variables. These constraints specify that the deformation at the support beam end points d_1 and d_2, as shown in Figure 11. These constraints are established in order to evaluate how much the beam will deform towards the battery cells when the battery box is subjected to a side impact.

Table 2 Design variables.

Design Variable	Initial Value	Variable Range	Type
Thickness, $\boldsymbol{t_1}$	1.5 mm	1 mm to 2 mm	Continuous
Thickness, $\boldsymbol{t_2}$	1.5 mm	1 mm to 2 mm	Continuous
Thickness, $\boldsymbol{t_3}$	1.5 mm	1 mm to 2 mm	Continuous
Length, $\boldsymbol{x_1}$	25 mm	21 mm to 29 mm	Continuous
Length, $\boldsymbol{x_2}$	18.91 mm	14.91 mm to 22.91 mm	Continuous
Length, $\boldsymbol{x_3}$	40.00 mm	36 mm to 44 mm	Continuous
Density, $\boldsymbol{\rho}$	0.34 g/cm^3	0.17, 0.34 and 0.54 g/cm^3	Discrete

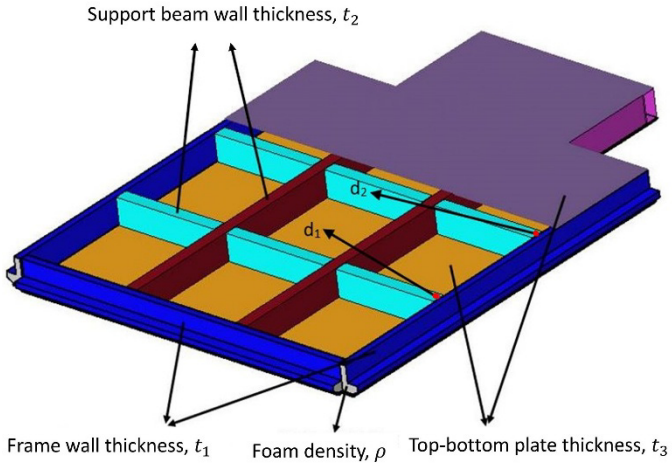

Figure 11 The representation of thickness and density design variables and constraints on the battery box.

The optimization process aims to maximize SEA and minimize PCF. A higher SEA value indicates the battery box's increased energy absorption capacity. Conversely, a lower PCF value indicates that the battery and surrounding components will be subjected to a lower peak force. Both objectives contribute to improving the battery box safety performance. Consequently, an equilibrium is sought in battery box optimization where SEA is minimized, and PCF is maximized. As a multi-objective optimization, the battery box optimization problem is expressed by the following:

$$\min\left\{-SEA\left(x_1,x_2,x_3,t_1,t_2,t_3,\rho\right),PCF\left(x_1,x_2,x_3,t_1,t_2,t_3,\rho\right)\right\}$$
$$\text{s.t.}\begin{Bmatrix} d_1,d_2 \le d_{\max},d_{\max} \in 25\text{mm},30\text{mm}, \\ 21\text{mm} \le x_1 \le 29\text{mm}, \\ 14.91\text{mm} \le x_2 \le 22.91\text{mm}, \\ 36\text{mm} \le x_3 \le 44\text{mm}, \\ 1\text{mm} \le t_i \le 2\text{mm}, \\ \rho \in 0.17,0.34.0.51 \end{Bmatrix} \tag{6}$$

3.2 Surrogate Models

In the crashworthiness optimization of the aluminum foam-filled battery box, surrogate models are employed instead of FE simulations with high computational costs. Surrogate models that approximate the response of complex simulations are, therefore, also called meta-models. This simplified representation allows for rapid and more efficient predictions in optimization processes. In order to achieve a successful result in the optimization process, it is essential to use a sufficiently representative surrogate model.

The initial step in surrogate modeling is to create the appropriate design space. At this stage, the ranges of input parameters and the target outputs corresponding to these are determined. The objective is to construct a comprehensive data set that can be used to develop a model capable of representing the behavior of the complex system. To obtain the data set required to build surrogate models, numerical simulations are performed for specific sample points within the design space. The Latin hypercube sampling (LHS) method is used to construct the design space in the multi-dimensional input parameter space, ensuring that the sample points are distributed homogeneously throughout the design space (McKay et al., 2000).

In engineering optimization, several surrogate modeling techniques have been widely adopted, including RSM (Myers et al., 2016), Kriging (Forrester et al., 2008), RBF (Buhmann, 2003), and SVR (Roy et al., 2019; Smola and Schölkopf, 2004). The RSM method employs polynomial functions to approximate the response surface of the simulation data, thereby providing a reasonably accurate model for problems exhibiting relatively smooth response surfaces. Kriging generates a more sophisticated surrogate model by modeling the response surface as a Gaussian process. In addition to generating precise predictions for the existing simulation data, the model also provides the uncertainties of these predictions, thus enabling an estimation of the model's reliability. By employing radial basis functions to interpolate the response surface of the simulation data, the RBF method can better represent nonlinear relationships in the data. The SVR method, which adapts the principles of support vector machines to regression problems, provides an effective solution for high-dimensional data and nonlinear problems.

The optimal parameters for surrogate models are identified using a hyperparameter search. This systematically varies each model's hyperparameters to find the most appropriate. For the RSM model, this is achieved by choosing different polynomial degrees: linear, quadratic and cubic. Within the Kriging model, the hyperparameter search is performed on the kernel parameters such as constant value, constant boundaries, length scale and length scale boundaries. Prediction performance for the RBF model is obtained for a range of alpha and gamma parameters. In the SVR model, a hyperparameter search is applied to the following parameters: gamma, epsilon, penalty parameter C, and kernel (linear, RBF, or sigmoid). The prediction accuracy of the surrogate models in the optimization process depends on their generalization capabilities. In order to measure the generalization performance and select the optimal parameters for each surrogate model, grid search and K-fold cross-validation with k=5 are utilized (Claesen and De Moor, 2015; Hastie et al., 2009). This ensures that each surrogate model is tailored to provide accurate predictions for the battery pack crashworthiness optimization problem. The specific hyperparameters and search ranges for each model are detailed in Table 3.

Table 3 Hyperparameter search ranges for surrogate models.

Model	Parameter	Search Range
RSM	degree of polynomial	$\{\mathbf{1}, \mathbf{2}, \mathbf{3}\}$
Kriging	constant value	$\{\mathbf{0.1}, \mathbf{0.316}, \mathbf{1.0}, \mathbf{3.162}, \mathbf{10}\}$
	constant bounds	$(\mathbf{10^{-3}}, \mathbf{10^{3}})$
	length scale	$\{\mathbf{0.1}, \mathbf{0.316}, \mathbf{1.0}, \mathbf{3.162}, \mathbf{10}\}$
	length scale bounds	$(\mathbf{10^{-2}}, \mathbf{10^{2}})$
RBF	alpha	$\{\mathbf{0.001}, \mathbf{0.01}, \mathbf{0.1}, \mathbf{1}, \mathbf{10}, \mathbf{100}\}$
	gamma	$\{\mathbf{0.01}, \mathbf{0.1}, \mathbf{1}, \mathbf{10}, \mathbf{100}\}$
SVR	kernel	$\{'\boldsymbol{linear}', '\boldsymbol{sigmoid}', '\boldsymbol{rbf}'\}$
	C	$\{\mathbf{0.001}, \mathbf{0.01}, \mathbf{0.1}, \mathbf{1}, \mathbf{10}, \mathbf{100}, \mathbf{1000}\}$
	epsilon	$\{\mathbf{0.0001}, \mathbf{0.001}, \mathbf{0.01}, \mathbf{0.1}, \mathbf{1}, \mathbf{10}\}$
	gamma	$\{\mathbf{0.0001}, \mathbf{0.001}, \mathbf{0.01}, \mathbf{0.1}, \mathbf{1}, \mathbf{10}\}$

4 RESULTS AND DISCUSSION

4.1 Performance Evaluation of Surrogate Models

In order to assess the predictive accuracy of surrogate models, several key performance indicators are employed. Coefficient of determination (R^2) measures the extent to which a model accounts for the variance in the dependent variable. A higher R^2 value indicates a better fit to the data set. Explained Variance evaluates the efficacy of a specified model in elucidating the observed variability within a given data set. Mean absolute error (MAE) represents the mean of the absolute differences between the predicted and actual values. In contrast, root mean square error (RMSE) is a more effective measure for identifying significant errors due to its quadratic nature. Mean absolute percentage error (MAPE) allows an intuitive comparison of model performance by presenting prediction errors as percentages.

This study considers a multi-objective optimization problem in which two objective functions, PCF and SEA, are simultaneously optimized, while deformations d_1 and d_2 are required to satisfy specified constraints. The primary objective of this section is to evaluate the representational capabilities of different surrogate models and determine the model that most accurately predicts the system behavior across the design space. In order to reduce the relative error between optimization results and FE analysis, the best surrogate model should represent the objective functions and constraints. A total of 120 sample points in the entire design space are identified by the LHS method for constructing surrogate models. FE analyses are performed on these sample points to obtain the corresponding system responses. Comparison of the surrogate model performances in predicting PCF, SEA, and deformation constraints, d_1 and d_2, are presented in Figure 12, with the detailed numerical values provided in Table A1 in appendix.

The previously discussed metrics, including R^2, explained variance, RMSE, MAE, and MAPE, are employed to evaluate the models. By the R^2 metric, the ranking of surrogate modeling algorithms in terms of their performance in predicting PCF, SEA, d_1 and d_2 is presented in Table 4. High R^2 values indicate that the evaluated surrogate models accurately capture the relationships between design variables and optimization objectives and are sufficiently representative for optimizing the system. A comprehensive evaluation of the prediction performance confirms that SVR is the optimal surrogate model for predicting PCF and SEA, achieving remarkable R^2 values of 0.905 and 0.977, respectively. For the deformation constraints d_1 and d_2, RBF emerges as the superior choice, as reflected in its R^2 values of 0.937 and 0.949, making it the most reliable option for these specific outputs. The efficacy of SVR and RBF in modeling complex dependencies and localized non-linear relationships is emphasized by the findings, thereby supporting their applicability in this study.

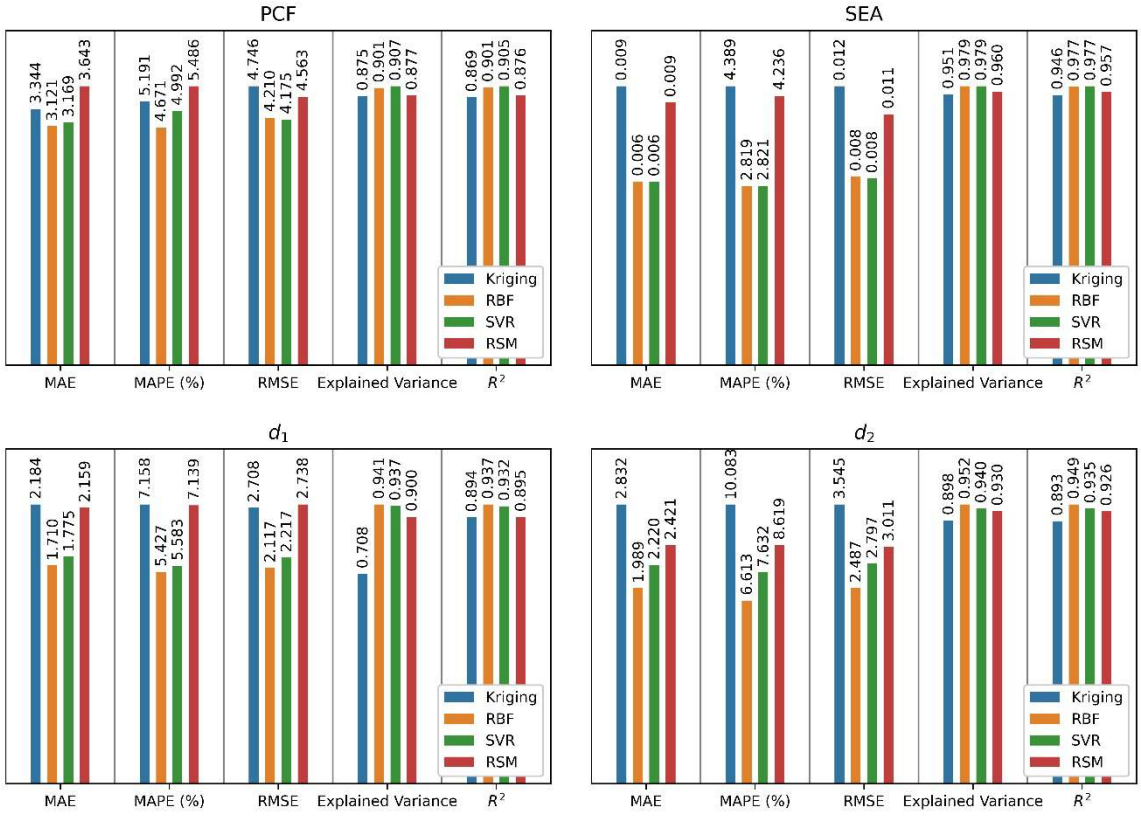

Figure 12 *Comparison of surrogate model performances for the objective function SEA, PCF, and deformation c*

Table 4 Ranking of surrogate model performance for the objective function PCF, SEA, and deformation constraints d_1 and d_2 using the R^2 metric.

	Higher to lower performance			
Target	**1**	**2**	**3**	**4**
PCF	SVR	RBF	RSM	Kriging
SEA	SVR	RBF	RSM	Kriging
$\boldsymbol{d_1}$	RBF	SVR	RSM	Kriging
$\boldsymbol{d_2}$	RBF	SVR	RSM	Kriging

4.2 Optimization Results

In the literature, multi-objective optimization problems are frequently addressed using established methods such as NSGA-II (Pang et al., 2017; Liao et al., 2008) and MOPSO (Sun et al., 2010; Xiao et al., 2015). This research employs the NSGA-II algorithm, initially introduced by Deb et al. (2002), to identify the optimal solution, selected for its swift convergence and its proficiency in producing well-distributed Pareto fronts. The key parameters, including population size, number of offsprings, and crossover probability, are detailed in Table 5. Furthermore, the performance of NSGA-II is compared to MOPSO under identical conditions. While both algorithms yield comparable SEA values for DC25, NSGA-II shows a significant runtime advantage, completing the optimization in about a third of the time required by MOPSO. For DC30, NSGA-II not only achieves a shorter runtime, but also a slightly better optimization result. These results, summarized in Table 6, highlight that NSGA-II provides better optimization results and computational efficiency for this study, making it the more appropriate choice for the defined objectives and constraints. Figure 13 shows the Pareto fronts for the optimization problem, where the deformation constraints d_1 and d_2 are represented by DC25 and DC30, corresponding to limits of 25 mm and 30 mm, respectively. In this notation, “DCXX” indicates the deformation constraints applied during the optimization process, where “XX” represents the specific value of the constraints in millimeters. For example, “DC25” means that both d_1 and d_2 are set to 25 mm. These Pareto fronts illustrate the optimal boundaries in the design space and provide designers with valuable insight into the trade-offs between different objectives under varying deformation constraints. Consistent with previous studies, PCF and SEA are found to be two competing objectives in this study. This conflict is manifested in the positive correlation between PCF and SEA, where an increase in PCF is typically accompanied by a

corresponding increase in SEA. In the crashworthiness optimization of the battery box, the aim is to maximize the SEA while minimizing the PCF. Since optimization algorithms are inherently designed to minimize objective functions, SEA is used in the optimization process by taking its negative value to comply with this framework. Each point on the Pareto front represents an optimal solution to the optimization problem as determined by the optimization algorithm. The selection of the optimum point depends on the balance between maximizing SEA and minimizing PCF, guided by the design priorities. If higher PCF values are acceptable, solutions from the upper part of the Pareto front are appropriate, while solutions from the lower part are preferable if minimizing PCF is a priority.

Table 5 Parameters of the NSGA-II algorithm used in the optimizations.

Parameter	Value
Population size	1000
Number of offsprings	100
Crossover probability	0.9
Crossover distribution index	15
Mutation distribution index	20
Parameter	Value

Table 6 Comparison of optimization results for MOPSO and NSGA-II

Algorithm	DC25			DC30		
	SEA (kJ/kg)	PCF (kN)	Runtime (s)	SEA (kJ/kg)	PCF (kN)	Runtime (s)
MOPSO	0.307	64.969	123	0.317	64.994	123
NSGA-II	0.307	64.987	35	0.325	64.966	33

An analysis of the Pareto front curves obtained from the optimization with varying deformation constraints d_1 and d_2 reveals that when these constraints are set to higher limits, the battery box exhibits both increased SEA and elevated PCF values. With higher deformation constraints, the structure can undergo greater deformation and thus absorb more energy. This increased energy absorption is primarily due to a larger portion of the energy being dissipated through plastic deformation, leading to higher SEA values. For the same PCF value, this increased energy absorption is directly related to the improved deformability of the system. Thus, allowing for greater flexibility in deformation enables the structure to absorb more energy effectively. On the other hand, when examining the Pareto front within lower PCF values, it is observed that changes in the d_1 and d_2 constraints do not significantly affect the energy absorption capacity. This is because, at these lower PCF values, the structure's energy absorption mechanisms, such as plastic deformation or buckling, are not constrained by the deformation limits. In essence, the structure already has sufficient deformation capacity to absorb energy, so changing the d_1 and d_2 constraints does not make a noticeable difference in energy absorption at these lower PCF values.

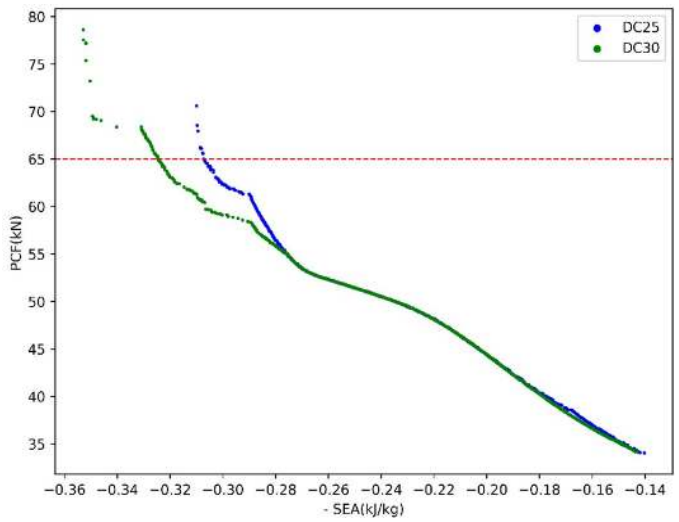

Figure 13 The Pareto fronts for the optimization problem, with deformation constraints d_1 and d_2 represented by DC25 and DC30, correspond to limits of 25 mm and 30 mm, respectively.

In the scenario where the PCF is required to be limited to below 65 kN, the Pareto points corresponding to the optimal design solutions are indicated by the red line in Figure 13. Table 7 gives the initial and predicted optimal design variables for the case where the PCF is constrained to be less than 65 kN. Table 8 provides the corresponding optimization and FE analysis results, including the relative errors. Both tables show the initial design and the optimized scenarios DC25 and DC30, demonstrating how the optimization process improves the performance metrics compared to the initial design.

Table 7 Initial and optimal design variables for the case where PCF < 65 kN.

Design Variable	Initial Values	DC25	DC30
t_1 [mm]	1.500	2.000	1.998
t_2 [mm]	1.500	1.992	1.410
t_3 [mm]	1.500	1.002	1.000
x_1 [mm]	25.000	28.760	21.318
x_2 [mm]	18.910	15.970	15.148
x_3 [mm]	40.000	42.157	36.168
ρ [g/cm^3]	0.34	0.17	0.34

Table 8 Optimization results, including FE analysis and relative errors, for the case where PCF < 65 kN.

Targets	Initial Values	DC25			DC30		
		Opt.	FEA	RE (%)	Opt.	FEA	RE (%)
SEA (kJ/kg)	0.211	0.307	0.297	3.35	0.325	0.318	2.04
PCF (kN)	72.830	64.987	66.679	2.61	64.966	64.409	0.90
d_1 (mm)	28.630	24.999	24.019	3.92	29.365	30.331	3.29
d_2 (mm)	28.500	14.765	14.199	3.83	19.592	20.929	6.82

In comparison to the initial design of the aluminum foam-filled battery box, for the deformation constraints d_1 and d_2 with a value of 25 mm (DC25), SEA improves by 40.76%, increasing from 0.211 kJ/kg to 0.297 kJ/kg, while PCF decreases by 8.45%. When the deformation constraints are defined as 30 mm (DC30), SEA demonstrates a 50.71% improvement, rising from 0.211 kJ/kg to 0.318 kJ/kg, accompanied by an 11.56% reduction in PCF. The maximum relative error for the optimization outputs SEA, PCF, and constraints d_1 and d_2 are observed as 3.35%, 2.61%, 3.92%, and 6.82%, respectively. Similarly, the MAPE values for the surrogate models used in the optimization are shown in Fig. 10 for PCF, SEA, d_1 and d_2, with values of 4.67%, 2.82%, 5.47%, and 6.61%. Consequently, the relative error values between the optimization results and FEA are within expected ranges, demonstrating that the optimal results are achieved with a high degree of accuracy. The deformation modes of the optimal structures in consequence of the crash simulation are illustrated in Figure 14.

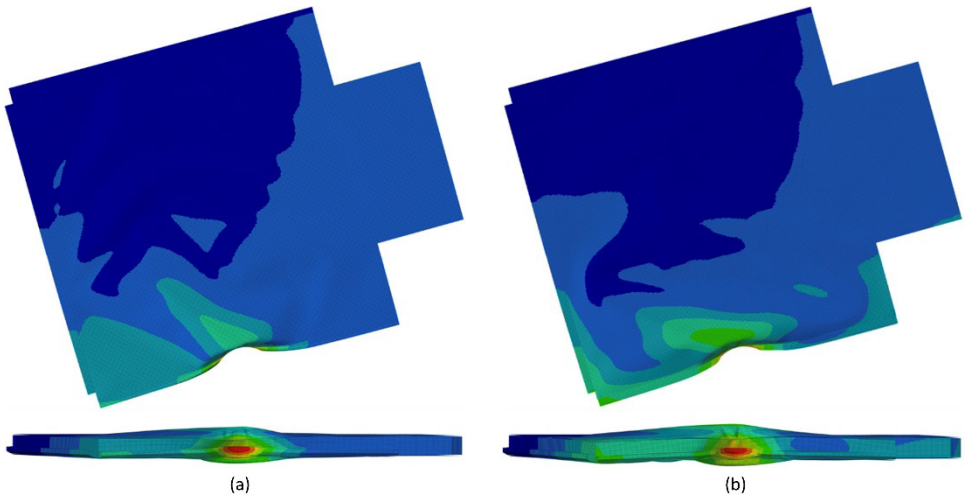

Figure 14 *Top and side view of post-crash deformation, (a) DC25 optimal, (b) DC30 optimal.*

5 CONCLUSION

This study aimed to optimize the crashworthiness of aluminum foam-filled battery boxes for electric vehicles under side pole impact conditions, an area that has seen relatively few studies compared to traditional axial crushing analyses. By employing a multi-objective optimization framework with the NSGA-II algorithm, the study focused on improving specific energy absorption (SEA) and reducing peak crushing force (PCF) – typically conflicting goals in crashworthiness optimization. Seven key design variables are investigated, including the wall thicknesses of the structural components, the aluminum foam density, and the cross-sectional dimensions of the side frame. A unique aspect of this research is the use of three different aluminum foam densities as design variables, offering flexibility in controlling deformation under varying impact conditions. The performances of RSM, Kriging, RBF and SVR surrogate models are evaluated to capture the complex relationships between design variables and crash outcomes. The optimization framework presented here provides valuable insights for the development of safer and more efficient battery enclosures in electric vehicle designs. Key findings from this study include:

- As a result of the multi-objective optimization, significant improvements in both SEA and PCF were achieved. For the DC25 constraint, the SEA increased by 40.76%, from 0.211 kJ/kg to 0.297 kJ/kg, while the PCF decreased by 8.45%, from 63.56 kN to 58.20 kN. Similarly, under the DC30 constraint, the SEA improved by 50.71%, reaching 0.318 kJ/kg, and the PCF was reduced by 11.56%, dropping to 56.16 kN. These results demonstrate the effectiveness of the optimization framework in enhancing crashworthiness performance by balancing energy absorption and peak force reduction.
- The best crash strength is obtained for both the DC25 and DC30 boundary conditions when the wall thickness of the frame plate is at the upper limit and the thickness of the bottom-up plates is at the lower limit. On the other hand, the optimum wall thickness value of the support beam is found to be dependent on the deformation constraint.
- In the case where a smaller amount of collapse is required (DC25), the side frame lengths x_1 and x_3 increased and 0.17gr/cm^3 density aluminum foam gave better results within the enlarged area. On the contrary, in the case where more collapse occurred (DC30), the lengths of the side frames x_1 and x_3 decreased and accordingly the use of aluminum foam with a density of 0.34gr/cm^3 in the shrinking volume gave the optimal result. The variable x_2 is close to the lower limit in both cases according to the initial design.
- The surrogate model performance analysis revealed that SVR and RBF are the most accurate surrogate models for the objective functions and deformation constraints, respectively.

The key finding of this study is that optimizing the structural design of aluminum foam-filled battery enclosures for electric vehicles significantly enhances their crashworthiness under side pole impact conditions, addressing a critical aspect of EV safety.

Further experimental studies are necessary to validate the findings of this study and assess their applicability under diverse real-world conditions.

Author's Contribuitions: Conceptualization: İsmail Yay, Ahmet Remzi Özcan and Emre Demirci; Methodology: İsmail Yay, Ahmet Remzi Özcan and Emre Demirci; Investigation: İsmail Yay, Ahmet Remzi Özcan and Emre Demirci; Writing - original draft: İsmail Yay, Ahmet Remzi Özcan and Emre Demirci; Writing: Ahmet Remzi Özcan and Emre Demirci; Supervision: Emre Demirci.

Editor: Marco L. Bittencourt

REFERENCES

Abdullah, N., Sani, M., Salwani, M., Husain, N. (2020). A review on crashworthiness studies of crash box structure. Thin-Walled Structures, 153, 106795.

Acar, E., Altin, M., Güler, M. A. (2019). Evaluation of various multi-cell design concepts for crashworthiness design of thin-walled aluminum tubes. Thin-Walled Structures, 142, 227-235.

Ahmad, Z. and Thambiratnam, D. (2009). Crushing response of foam-filled conical tubes under quasi-static axial loading. Materials & Design, 30(7), 2393–2403.

Albak, E. İ. (2021). Multi-objective crashworthiness optimization of thin-walled multi-cell tubes with different wall lengths. International Journal of Crashworthiness, 26(4), 438–455.

Albak, E. İ. (2023). Optimization design for circular multi-cell thin-walled tubes with discrete and continuous design variables. Mechanics of Advanced Materials and Structures, 30(24), 5091–5105.

Altair Hyperworks. (2019). Radioss user guide.

Altin, M., Güler, M. A., Mert, S. K. (2017). The effect of percent foam fill ratio on the energy absorption capacity of axially compressed thin-walled multi-cell square and circular tubes. International Journal of Mechanical Sciences, 131, 368–379.

Altin, M., Acar, E., Güler, M. A. (2018). Foam filling options for crashworthiness optimization of thin-walled multi-tubular circular columns. Thin-Walled Structures, 131, 309-323.

An, Y., Wen, C. E., Hodgson, P. D., Yang, C. H. (2012). Impact response and energy absorption of aluminium foam-filled tubes. Applied Mechanics and Materials, 152, 436–439.

Arora, S., Shen, W., Kapoor, A. (2016). Review of mechanical design and strategic placement technique of a robust battery pack for electric vehicles. Renewable and Sustainable Energy Reviews, 60, 1319–1331.

Bala, A. and Chaitanya Kamaraju, M. (2020). Design and optimization of battery housing in electric cars [Master's thesis in Product Development]. Chalmers University of Technology.

Baumeister, J., Weise, J., Hirtz, E., Höhne, K., Hohe, J. (2014). Applications of aluminum hybrid foam sandwiches in battery housings for electric vehicles. Procedia Materials Science, 4, 317–321.

Bidadi, J., Hampaiyan Miandowab, H., Saeidi Googarchin, H., Akhavan-Safar, A., Silva, L. da. (2024). Experimental and numerical investigation on the crashworthiness performance of double hat-section al-CFRP beam subjected to quasi-static bending test. Polymer Composites, 45(6), 5656–5674.

Biharta, M. A. S., Santosa, S. P., Widagdo, D., Gunawan, L. (2022). Design and optimization of lightweight lithium-ion battery protector with 3D auxetic meta structures. World Electric Vehicle Journal, 13(7), 118.

Buhmann, M. D. (2003). Radial basis functions: Theory and implementations (1st ed.). Cambridge University Press, Cambridge, UK.

Chen, J. (2023). Research on aluminum alloy materials and application technology for automotive lightweighting. J. Mater. Chem, 4, 1–7.

Claesen, M. and De Moor, B. (2015). Hyperparameter search in machine learning. arXiv Preprint arXiv:1502.02127.

Deb, K., Pratap, A., Agarwal, S., Meyarivan, T. (2002). A fast and elitist multiobjective genetic algorithm: NSGA-II. IEEE Transactions on Evolutionary Computation, 6(2), 182–197.

Demirci, E., and Yıldız, A. R. (2018). An investigation of the crash performance of magnesium, aluminum and advanced high strength steels and different cross-sections for vehicle thin-walled energy absorbers. Materials Testing, 60(7-8), 661–668.

Djamaluddin, F., Abdullah, S., Ariffin, A. K., Nopiah, Z. M. (2016). Finite element analysis and crashworthiness optimization of foam-filled double circular under oblique loading. Latin American Journal of Solids and Structures, 13, 2176-2189.

Djamaluddin, F. (2024). Optimization of foam-filled crash-box under axial loading for pure electric vehicle. Results in Materials, 21, 100505.

Doruk, E. and Demir, S. (2024). New generation steels for light weight vehicle safety related applications. Materials Testing, 66(7), 992–998.

Erzincanlioğlu, S., Aydiner, T., Aras, F., Çelik, H., Billur, E., Karabulut, S., Gümüs, I. O. (2022). Development of new vehicle safety structures by using third-generation steels. SAE International Journal of Materials and Manufacturing, 15(2), 155–174.

Euro NCAP. (2015). Oblique pole side impact testing protocol (Version 7.0.2).

Fang, J., Sun, G., Qiu, N., Kim, N.-H., Li, Q. (2017). On design optimization for structural crashworthiness and its state of the art. Structural and Multidisciplinary Optimization, 55, 1091–1119.

Farzaneh, F., Zhang, Q., Jung, S. (2024). Enhancing electric vehicle battery safety and performance: Aluminum tubes filled with PCM. Journal of Energy Storage, 97, 112922.

Forrester, A., Sobester, A. Keane, A. (2008). Engineering design via surrogate modelling: A practical guide. John Wiley & Sons.

Fragoso-Medina, O. and Velázquez-Villegas, F. (2023). Aluminum foam to improve crash safety performance: A numerical simulation approach for the automotive industry. Mechanics Based Design of Structures and Machines, 51(7), 3583–3597.

Gao, Y. and Huaiwei, H. (2023). Energy absorption characteristics and optimization of three-beam star honeycomb. Mechanics of Advanced Materials and Structures, 30(8), 1559–1573.

Gong, C., Liu, J., Han, Y., Hu, Y., Yu, H., Zeng, R. (2021). Safety of electric vehicles in crash conditions: A review of hazards to occupants, regulatory activities, and technical support. IEEE Transactions on Transportation Electrification, 8(3), 3870–3883.

Hanssen, A., Hopperstad, O. S., Langseth, M., Ilstad, H. (2002). Validation of constitutive models applicable to aluminium foams. International Journal of Mechanical Sciences, 44(2), 359–406.

Hastie, T., Tibshirani, R., Friedman, J. H. (2009). The elements of statistical learning: Data mining, inference, and prediction (2nd ed.). Springer, New York, NY.

Huang, H., Yang, X., Yan, Q., Xiang, Z., Xu, S. (2022). Crashworthiness analysis and multiobjective optimization of bio-inspired sandwich structure under impact load. Thin-Walled Structures, 172, 108840.

Kokkula, S., Langseth, M., Hopperstad, O. S., Lademo, O. G. (2006). Behaviour of an automotive bumper beam-longitudinal system at 40% offset impact: An experimental and numerical study. Latin American Journal of Solids and Structures, 3(1), 59–73.

Kovács, J. and Lukács, J. (2022). Investigation of the possibility for compensating the HAZ softening of AA7075-T6. Periodica Polytechnica Mechanical Engineering, 66(3), 207–212.

Kurtaran, H., Eskandarian, A., Marzougui, D., Bedewi, N. (2002). Crashworthiness design optimization using successive response surface approximations. Computational Mechanics, 29, 409–421.

Li, K., Feng, Y., Gao, Y., Zheng, H., Qiu, H. (2020). Crashworthiness optimization design of aluminum alloy thin-walled triangle column based on bioinspired strategy. Materials, 13(3), 666.

Li, T., Peng, Y., Qiao, Y., Zhu, W., Zhang, J., Wang, K., Xie, G., Zhang, H. (2024a). Experimental study on crashworthiness and lightweight of cutting-type energy-absorbing structure of magnesium alloy for trains. Engineering Structures, 301, 117287.

Li, M., Sang, L., Liu, Z., Duan, S., Hou, W. (2024b). Crashworthiness optimization of variable stiffness b-pillar with thermoplastic composites. International Journal of Mechanical Sciences, 109457.

Liao, X., Li, Q., Yang, X., Zhang, W., Li, W. (2008a). Multiobjective optimization for crash safety design of vehicles using stepwise regression model. Structural and Multidisciplinary Optimization, 35, 561–569.

Liao, X., Li, Q., Yang, X., Wei, L., Zhang, W. (2008b). A two-stage multi-objective optimisation of vehicle crashworthiness under frontal impact. International Journal of Crashworthiness, 13(3), 279–288.

Linul, E., Pietras, D., Sadowski, T., Marşavina, L., Rajak, D. K., Kovacik, J. (2021). Crashworthiness performance of lightweight composite metallic foams at high temperatures. Composites Part A: Applied Science and Manufacturing, 149, 106516.

Liu, Z., Zhu, C., Zhu, P., Chen, W. (2018). Reliability-based design optimization of composite battery box based on modified particle swarm optimization algorithm. Composite Structures, 204, 239–255.

Magliaro, J., Altenhof, W., Alpas, A. T. (2022). A review of advanced materials, structures and deformation modes for adaptive energy dissipation and structural crashworthiness. Thin-Walled Structures, 180, 109808.

Marzougui, D., Samaha, R. R., Nix, L., Kan, C. D. S. (2013). Extended validation of the finite element model for the 2010 toyota yaris passenger sedan (MASH 1100kg vehicle) (Technical Report 13-2567).

McKay, M. D., Beckman, R. J., Conover, W. J. (2000). A comparison of three methods for selecting values of input variables in the analysis of output from a computer code. Technometrics, 42(1), 55–61.

Meriç, D. and Gedikli, H. (2022). Multi-objective optimization of energy absorbing behavior of foam-filled hybrid composite tubes. Composite Structures, 279, 114771.

Mou, H. L., Zou, T. C., Feng, Z. Y., Xie, J. I. A. N. G. (2016). Crashworthiness analysis and evaluation of fuselage section with sub-floor composite sinusoidal specimens. Latin American Journal of Solids and Structures, 13(6), 1186-1202.

Myers, R. H., Montgomery, D. C., Anderson-Cook, C. M. (2016). Response surface methodology: Process and product optimization using designed experiments (4th ed.). John Wiley & Sons, Hoboken, NJ.

Navale, A., Chippa, S., Chougule, D., Raut, P. (2021). Crashworthiness aspects of electric vehicle design. International Journal of Crashworthiness, 26(4), 368–387.

Neu, T., Heim, K., Seeliger, W., Kamm, P., García-Moreno, F. (2024). Aluminum foam sandwiches: A lighter future for car bodies. JOM, 76(5), 2619–2630.

Pang, T., Kang, H., Yan, X., Sun, G., Li, Q. (2017). Crashworthiness design of functionally graded structures with variable diameters. International Journal of Crashworthiness, 22(2), 148–162.

Peroni, L., Avalle, M., Peroni, M. (2008). The mechanical behaviour of aluminium foam structures in different loading conditions. International journal of impact engineering, 35(7), 644-658.

Qiao, W., Zhang, Z., Lu, D., Yu, L. (2021). Study on side collision of battery boxes based on HyperWorks. Journal of Physics: Conference Series, 2137, 012012.

Raponi, E., Bujny, M., Olhofer, M., Aulig, N., Boria, S., Duddeck, F. (2019). Kriging-assisted topology optimization of crash structures. Computer Methods in Applied Mechanics and Engineering.

Reyes, A., Hopperstad, O. S., Berstad, T., Hanssen, A. G., Langseth, M. (2003). Constitutive modeling of aluminum foam including fracture and statistical variation of density. European Journal of Mechanics-A/Solids, 22(6), 815–835.

Roy, A., Manna, R. and Chakraborty, S. (2019). Support vector regression based metamodeling for structural reliability analysis. Probabilistic Engineering Mechanics, 55, 78–89.

Saber, A., Güler, M. A., Altin, M., Acar, E. (2024). Bio-inspired thin-walled energy absorber adapted from the xylem structure for enhanced vehicle safety. Brazilian Society of Mechanical Sciences and Engineering.

Safari, H., Nahvi, H., Esfahanian, M. (2018). Improving automotive crashworthiness using advanced high strength steels. International Journal of Crashworthiness, 23(6), 645–659.

Setiawan, R. and Salim, M. R. (2017). Crashworthiness design for an electric city car against side pole impact. Journal of Engineering & Technological Sciences, 49(5).

Sharma, D. K. and Prabhakar, A. (2021). A review on air cooled and air centric hybrid thermal management techniques for li-ion battery packs in electric vehicles. Journal of Energy Storage, 41, 102885.

Sharma, S. S., Yadav, S., Joshi, A., Goyal, A., Khatri, R. (2022). Application of metallic foam in vehicle structure: A review. Materials Today: Proceedings, 63, 347–353.

Smola, A. J. and Schölkopf, B. (2004). A tutorial on support vector regression. Statistics and Computing, 14, 199–222.

Sun, G., Li, G., Stone, M., & Li, Q. (2010). A two-stage multi-fidelity optimization procedure for honeycomb-type cellular materials. Computational Materials Science, 49(3), 500–511.

Sun, G., Li, G., Zhou, S., Li, H., Hou, S., Li, Q. (2011). Crashworthiness design of vehicle by using multiobjective robust optimization. Structural and Multidisciplinary Optimization, 44, 99–110.

Sun, G., Tian, J., Liu, T., Yan, X., Huang, X. (2018). Crashworthiness optimization of automotive parts with tailor rolled blank. Engineering Structures, 169, 201–215.

Victor Chombo, P., Laoonual, Y., Wongwises, S. (2021). Lessons from the electric vehicle crashworthiness leading to battery fire. Energies, 14(16), 4802.

Wang, D., Xu, P., Yang, C., Xiao, X., Che, Q. (2023). Crashing performance and multi-objective optimization of honeycomb-filled thin-walled energy absorber with axisymmetric thickness. Mechanics of Advanced Materials and Structures, 30(11), 2203–2220.

Wang, H., Wang, Z., Fan, Y., Gao, Q., Wang, H. (2024). Multi-objective lightweight design of automotive battery pack box for crashworthiness. International Journal of Crashworthiness, 29(2), 292–307.

White, M. and Jones, N. (1999). Experimental quasi-static axial crushing of top-hat and double-hat thin-walled sections. International Journal of Mechanical Sciences, 41(2), 179–208.

Xiao, Z., Fang, J., Sun, G., Li, Q. (2015). Crashworthiness design for functionally graded foam-filled bumper beam. Advances in Engineering Software, 85, 81–95.

Yang, N., Fang, R., Li, H., Xie, H. (2019). Dynamic and static analysis of the battery box structure of an electric vehicle. IOP Conference Series: Materials Science and Engineering, 688, 033082.

Yao, R., Pang, T., Zhang, B., Fang, J., Li, Q., Sun, G. (2023). On the crashworthiness of thin-walled multi-cell structures and materials: State of the art and prospects. Thin-Walled Structures, 189, 110734.

Yildirim, A., Demirci, E., Karagöz, S., Özcan, Ş., Yildiz, A. R. (2023). Experimental and numerical investigation of crashworthiness performance for optimal automobile structures using response surface methodology and oppositional based learning differential evolution algorithm. Materials Testing, 65(3), 346–363.

Yıldız, B. S. (2020). Slime mould algorithm and kriging surrogate model-based approach for enhanced crashworthiness of electric vehicles. International Journal of Vehicle Design, 83(1), 54–68.

Yu, W. and Jiang, L. (2024). Application of carbon fiber reinforced aluminum matrix composites in automotive industry. International Journal of Automotive Manufacturing and Materials, 3–3.

Zhou, G., Yan, P., Wang, Q., Dai, S., Li, X., Hao, Y., Wang, Y. (2022). Optimal design of a novel crash box with functional gradient negative poisson's ratio structure. Proceedings of the Institution of Mechanical Engineers, Part D: Journal of Automobile Engineering, 236(14), 3309–3325.

APPENDIX: Performance comparison of surrogate models

Table A1 Comparison of surrogate models based on performance metrics for objective functions SEA, PCF, and deformation *constraints* d_1 and d_2.

Target	Model	MAE	MAPE (%)	EV	RMSE	R^2
PCF	Kriging	3.344	5.191	0.875	4.746	0.869
	RBF	3.121	4.671	0.901	4.210	0.901
	SVR	3.169	4.992	0.907	4.175	**0.905**
	RSM	3.643	5.486	0.877	4.563	0.876
SEA	Kriging	0.009	4.389	0.951	0.0117	0.946
	RBF	0.006	2.819	0.979	0.0079	**0.977**
	SVR	0.006	2.821	0.979	0.0078	**0.977**
	RSM	0.009	4.236	0.960	0.0106	0.957
d_1	Kriging	2.184	7.158	0.900	2.708	0.894
	RBF	1.710	5.427	0.941	2.117	**0.937**
	SVR	1.775	5.583	0.937	2.217	0.932
	RSM	2.159	7.139	0.900	2.738	0.895
d_2	Kriging	2.832	10.083	0.898	3.545	0.893
	RBF	1.989	6.613	0.952	2.487	**0.949**
	SVR	2.220	7.632	0.940	2.797	0.935
	RSM	2.421	8.619	0.930	3.011	0.926